Computation of Highly Swirling Confined Flow with a Reynolds Stress Turbulence Model

S. Hogg* and M. A. Leschziner†
University of Manchester, Manchester, England, United Kingdom

This paper addresses the problem of computing a strongly swirling confined turbulent flow akin to that encountered in combustors. The flow considered is unusual in that swirl reduces the level of turbulent transport to such a low level as to cause the flow to become subcritical, in the same sense as free-surface water flow at low Froude numbers. The ability of the turbulence model to capture the interaction between swirl and the turbulent stress field is, therefore, crucial to the predictive performance of the computational scheme as a whole. A finite-volume procedure is used here to contrast the performance of the k-ϵ eddy-viscosity model with that of a Reynolds-stress transport closure. It is shown that the former returns a seriously excessive level of turbulent diffusion and misrepresents the experimentally observed flow characteristics. In contrast, the Reynolds-stress model successfully captures the subcritical nature of the flow by returning significantly lower levels of the shear stress components and predicts velocity and turbulence fields that are in good agreement with corresponding measurements.

Nomenclature

$C_1, C_2, C_1',$ $C_2', C_\mu, C_k,$ $C_\epsilon, C_{D,1}, C_{D,2}$	= turbulence-model constants
d	= central-jet diameter at inlet
f_ℓ	= wall-distance functions in turbulence model
k	= turbulence energy
ℓ_m	= mixing length
m	= iteration level
n_i	= unit vector in direction i normal to a wall
P	= static pressure
P_{ij}	= production of stress $\overline{u_i u_j}$
r	= radial coordinate
r_a	= radius of forced-vortex flow core
R	= outer radius of confining flow chamber
R_{ij}	= additive contributions to stress-transport equations
S	= swirl parameter
S_ϕ	= source term related to property ϕ
$S_{ij}, S_{U,ij}, S_{P,ij}$	= source terms of stress $\overline{u_i u_j}$
U_i, U, V, W	= mean-flow velocity components
$\overline{u_i u_j}, \overline{u^2}, \overline{v^2}, \overline{w^2},$ $\overline{uv}, \overline{uw}, \overline{vw}$	= turbulent stresses
x	= axial coordinate
α	= relaxation parameter
δ_{ij}	= Kronecker delta
ϵ	= turbulence-energy dissipation
κ	= von Kármán constant
μ	= dynamic viscosity
ϕ	= general flow property
Φ_{ij}	= pressure-strain term in turbulence model
ρ	= fluid density
ω	= rotational speed

Introduction

SWIRL is commonly imparted to flows entering furnace and jet-engine combustors in order to enhance flame stability and mixing. The former objective is achieved through swirl, or rather its streamwise decay, producing an adverse pressure gradient that either increases recirculation, if this is already present due to a baffle, or provokes it, if swirl is sufficiently strong in the absence of such a baffle. Although this recirculation contributes to mixing indirectly through convective processes, the primary enhancement of mixing is assumed to result from the rotational shear strain generating higher levels of turbulence. This assumption is undoubtedly correct in many but not all flows, while in other cases it only holds in parts of the flow domain.

It is evident that any increase in shear strain will, in principle, tend to raise the level of transfer of mean kinetic energy to turbulence energy and increase the shear stresses through generation and/or redistribution processes. However, the turbulence field is also highly sensitive to a second swirl-related feature, namely, the body-force field resulting from the swirling motion, and this interaction may either amplify or strongly attenuate turbulent mixing, depending upon the radial variation of the swirl velocity, The mechanisms governing this interaction are complex but essentially rooted in uneven swirl-related contributions to the productions of the normal and shear stresses, involving products of the primary or secondary constituents of the rotational strain $(\partial W/\partial r - W/r)$ and different stresses. This selective "weighting" by the rotational terms tends to raise the level of normal-stress anisotropy and materially modifies the shear-stress field. It is thus observed that solid-body-type rotational motion provokes a reduction in the stresses, while free-vortex-type motion produces the opposite effect.

Most swirling flows combine both types of rotational motion: that in the inner region, bordering the centerline, is close to solid-body rotation, whereas the outer region, particularly if the flow is unconfined, is dominated by a free-vortex motion. Combustor flows are confined, of course, and the characteristics of their rotational field depend, apart from the swirl strength, primarily on the radius of the swirling stream's inlet relative to the radial extent of the confining chamber; the closer this ratio is to unity, the more the flow will tend to be dominated by solid-body-type motion, once the flow has progressed beyond an initial length downstream of the inlet. Moreover, the stronger the swirl is, the more pronounced will be the damping

effect of rotation on the turbulent transport. It follows, therefore, that swirl may, in fact, be detrimental to the desired operational performance of the combustor, and that the ability of a predictive procedure to describe the interaction between swirl and the turbulence field will determine its usefulness.

The present paper deals with the numerical calculation of a flow that falls into the above category of highly swirling, strongly confined configurations. The particular case chosen—a coaxial arrangement with a small nonswirling inner jet and a swirling outer annular jet—is, in fact, an extreme member of this group in that the inlet section admitting the swirling jet extends to the outer confining wall. In addition, swirl is so strong relative to the mean axial motion that the flow appears to lose its elliptic (viscous) character, due to a virtual collapse of turbulent exchange, and assumes hyperbolic properties.

Ignoring viscous effects, Benjamin[1,2] has presented an elegant analysis of this type of flow demonstrating that a close analogy exists between strongly swirling and free-surface flows. In particular, both flows display, in general, conjugate subcritical and supercritical regions, separated by a near-discontinuity that, in the case of free-surface flow, takes the form of a hydraulic jump, whereas the equivalent in the swirling flow is a vortex breakdown, manifesting itself through a recirculation bubble. In both cases, the subcritical region is one that permits the propagation of inertial disturbances from downstream to upstream regions, whereas the supercritical region, usually preceding the former, does not.

The importance of viscous processes in real turbulent flows and the influence of case-specific geometric parameters tend to blur somewhat Benjamin's clear-cut arguments when these are applied to practical situations. There is ample experimental evidence, however, that the arguments hold there too, at least qualitatively. Thus, Escudier and Keller[3] have performed a series of impressive experiments in highly swirling flows in long tubes, showing clearly the formation of a subcritical region downstream of a recirculation bubble. This region experienced hardly any axial variation, featured a near-stagnant or reverse-flow region at the axis of symmetry and permitted disturbances introduced far downstream to propagate backwards, resulting in a prominent distortion of the shape of the recirculation zone. Similarly, Jones and Wilhelmi[4] observed in a combustor-type geometry that, no matter how long the combustor was arranged to be, the flow behind the recirculation bubble, which contained a reverse-velocity region near the axis, could not be made to recover towards an undisturbed pipe flow.

The flow on which the present study focuses was examined by So et al.[5] and shows features very similar to those mentioned above; it has been chosen here in preference to the others because it was more comprehensively mapped and documented, particularly as regards turbulence quantities. The peculiar characteristics of the flow under consideration that, as pointed out, are closely related to the high degree of sensitivity of its turbulence structure to swirl-induced body forces, make it imperative that the turbulence model used to evaluate the turbulent stresses should contain an inherent mechanism capable of capturing this sensitivity without the need for ad hoc corrections. The lowest level of closure satisfying this requirement is one based on the solution of modeled equations for the Reynolds stresses. Such models either involve differential transport equations[6,7] or corresponding algebraic forms,[8,9] the latter based on the assumption that the convective plus diffusive transport of stresses is proportional to that of turbulence energy. Although both types of models have previously been used for computing swirling flow,[10-12] preference has been given to the computationally simpler algebraic variants.[10,11] A recent study by Fu et al.[13] has demonstrated, however, that an algebraic approximation of stress transport is inappropriate in the presence of swirl. It is primarily for this reason that a differential stress-transport model has been adopted here, and the paper proceeds to demonstrate that the model, in contrast to one based on an eddy-viscosity approach, correctly mimics the major characteristics of the present flow.

The Computational Approach

Mathematical Foundation

The flow considered is axially symmetric, steady, and assumed to have invariant fluid properties. Its mean field may thus be described by the two-dimensional versions of the time-averaged equations of continuity and momentum components, which may, respectively, be written as

$$\frac{\partial \rho U}{\partial x} + \frac{1}{r}\frac{\partial \rho r V}{\partial r} = 0 \tag{1}$$

$$\frac{\partial \rho r U\phi}{\partial x} + \frac{\partial \rho r V\phi}{\partial r} = \frac{\partial}{\partial x}\left(r\mu\frac{\partial\phi}{\partial x}\right) + \frac{\partial}{\partial r}\left(r\mu\frac{\partial\phi}{\partial r}\right) + rS_\phi \tag{2}$$

where ϕ stands for any of the momentum components U, V, and rW, and the corresponding sources S_ϕ are given in Table 1.

Turbulence effects are represented by Gibson and Launder's[6] simplified version of the high-Reynolds-number Reynolds-stress transport closure of Launder et al.[7] However, in order to highlight this model's performance, computations have also been performed with the standard k-ϵ model, as documented by Launder and Spalding.[14] The stress closure essentially consists of modeled transport equations for the stresses $\overline{u_i u_j}$ ($= \overline{u^2}$, $\overline{v^2}$, $\overline{w^2}$, $\overline{uv}$, $\overline{uw}$, $\overline{vw}$). A compact, yet reasonably transparent, presentation of the equations is one involving Cartesian tensor notation with terms arising from axial symmetry and swirl included as additive "corrections." This approach permits the equations to be written as

$$\frac{1}{r}\frac{\partial \rho r U_k \overline{u_i u_j}}{\partial x_k} - \frac{1}{r}\frac{\partial}{\partial x_k}\left(rC_k\rho\overline{u_k u_\ell}\frac{k}{\epsilon}\frac{\partial \overline{u_i u_j}}{\partial x_\ell}\right) = P_{ij} - \frac{2}{3}\rho\delta_{ij}\epsilon$$
$$+ \Phi_{ij} + R_{ij} \tag{3}$$

where U_k are mean-velocity components in the directions x_k,

$$P_{ij} \equiv -\rho\overline{u_i u_k}\frac{\partial U_j}{\partial x_k} - \rho\overline{u_j u_k}\frac{\partial U_i}{\partial x_k}$$

is the generation of the stress $\overline{u_i u_j}$, $\frac{2}{3}\delta_{ij}\epsilon$ stands for the (isotropic) rate of dissipation of normal stresses by the action of viscosity, and Φ_{ij} controls the redistribution of turbulence energy $k = \frac{1}{2}\overline{u_i u_i}$ among the normal stresses through the interaction of pressure and strain fluctuations. In the present model, the last term consists of three parts, namely,

"Rotta" stress-isotropization term:

$$\Phi_{ij,1} = -C_1\rho(\epsilon/k)\,[\overline{u_i u_j} - (\delta_{ij}/3)\overline{u_k u_k}] \tag{4}$$

"Rapid" isotropization-of-production term:

$$\Phi_{ij,2} = -C_2\rho\,[P_{ij} - (\delta_{ij}/3)P_{kk}] \tag{5}$$

Table 1   Sources of momentum equations

ϕ	S_ϕ
U	$-\dfrac{\partial P}{\partial x} - \dfrac{\partial \rho\overline{u^2}}{\partial x} - \dfrac{1}{r}\dfrac{\partial r\rho\overline{uv}}{\partial r}$
V	$-\dfrac{\partial P}{\partial r} + \dfrac{\rho W^2}{r} - \dfrac{\mu V}{r^2} - \dfrac{1}{r}\dfrac{\partial r\rho\overline{v^2}}{\partial r} - \dfrac{\partial \rho\overline{uv}}{\partial x} + \dfrac{\rho\overline{w^2}}{r}$
rW	$-\dfrac{2\mu}{r}\dfrac{\partial rW}{\partial r} - r\dfrac{\partial \rho\overline{uw}}{\partial x} - r\dfrac{\partial \rho\overline{vw}}{\partial r} - 2\rho\overline{vw}$

Table 2 Contributions R_{ij} to stress Eq. (3)

$\overline{u_i u_j}$	Convection	Production	Diffusion
$\overline{u^2}$	—	—	—
$\overline{v^2}$	$+2\rho\overline{vw}\dfrac{W}{r}$	$+2\rho\overline{vw}\dfrac{W}{r}$	$+2C_k\rho\dfrac{k}{\epsilon}\dfrac{(\overline{w^2})^2}{r^2} - 2\dfrac{\partial}{r\partial r}\left(C_k\rho\dfrac{k}{\epsilon}(\overline{vw})^2\right) - 2\dfrac{\partial}{\partial x}\left(C_k\rho\dfrac{k}{\epsilon}\overline{uw}\dfrac{\overline{vw}}{r}\right) - 2C_k\rho\dfrac{k}{\epsilon}\dfrac{\overline{w^2}}{r^2}\overline{v^2}$ $-2C_k\rho\dfrac{k}{\epsilon}\dfrac{\overline{uw}}{r}\dfrac{\partial\overline{vw}}{\partial x} - 2C_k\rho\dfrac{k}{\epsilon}\dfrac{\overline{vw}}{r}\dfrac{\partial\overline{vw}}{\partial r}$
$\overline{w^2}$	$-2\rho\overline{vw}\dfrac{W}{r}$	$-2\rho\overline{w^2}\dfrac{V}{r}$	$+2C_k\rho\dfrac{k}{\epsilon}\overline{w^2}\dfrac{\overline{v^2}}{r^2} + 2\dfrac{\partial}{r\partial r}\left(C_k\rho\dfrac{k}{\epsilon}(\overline{vw})^2\right) + 2\dfrac{\partial}{\partial x}\left(C_k\rho\dfrac{k}{\epsilon}\overline{uw}\dfrac{(\overline{vw})}{r}\right) - 2C_k\rho\dfrac{k}{\epsilon}\dfrac{(\overline{w^2})^2}{r^2}$ $+2C_k\rho\dfrac{k}{\epsilon}\dfrac{\overline{uw}}{r}\dfrac{\partial\overline{vw}}{\partial x} + 2C_k\rho\dfrac{k}{\epsilon}\dfrac{1}{r}\overline{vw}\dfrac{\partial\overline{vw}}{\partial r}$
$\overline{uv}$	$+\rho\overline{uw}\dfrac{W}{r}$	$+\rho\overline{uw}\dfrac{W}{r}$	$-C_k\rho\dfrac{k}{\epsilon}\overline{w^2}\dfrac{\overline{uv}}{r^2} - \dfrac{\partial}{\partial x}\left(C_k\rho\dfrac{k}{\epsilon}\dfrac{(\overline{uw})^2}{r}\right) - \dfrac{\partial}{r\partial r}\left(C_k\rho\dfrac{k}{\epsilon}\overline{vw}\,\overline{uw}\right)$ $-C_k\rho\dfrac{1}{r}\dfrac{k}{\epsilon}\left(\overline{uw}\dfrac{\partial\overline{uw}}{\partial x} + \overline{vw}\dfrac{\partial\overline{uw}}{\partial r}\right)$
$\overline{vw}$	$-\rho(\overline{v^2}-\overline{w^2})\dfrac{W}{r}$	$-\rho\overline{vw}\dfrac{V}{r} + \rho\overline{w^2}\dfrac{W}{r}$	$+C_k\rho\dfrac{k}{\epsilon}\dfrac{1}{r}\overline{vw}\dfrac{\partial}{\partial r}(\overline{v^2}-\overline{w^2}) + \dfrac{\partial}{\partial x}\left(C_k\rho\dfrac{k}{\epsilon}\overline{uw}\dfrac{(\overline{v^2}-\overline{w^2})}{r}\right)$ $+\dfrac{\partial}{r\partial r}\left(C_k\rho\dfrac{k}{\epsilon}\overline{vw}(\overline{v^2}-\overline{w^2})\right) - 4C_k\rho\dfrac{k}{\epsilon}\dfrac{1}{r}\overline{vw}\dfrac{\overline{w^2}}{r} + C_k\rho\dfrac{1}{r}\dfrac{k}{\epsilon}\overline{uw}\dfrac{\partial(\overline{v^2}-\overline{w^2})}{\partial x}$
$\overline{uw}$	$-\rho\overline{uv}\dfrac{W}{r}$	$-\rho\overline{uw}\dfrac{V}{r}$	$+C_k\rho\dfrac{k}{\epsilon}\dfrac{1}{r}\overline{vw}\dfrac{\partial\overline{uv}}{\partial r} + \dfrac{\partial}{\partial x}\left(C_k\rho\dfrac{k}{\epsilon}\overline{uw}\dfrac{\overline{uv}}{r}\right) + \dfrac{\partial}{r\partial r}\left(C_k\rho\dfrac{k}{\epsilon}\overline{vw}\,\overline{uv}\right) + C_k\rho\dfrac{k}{\epsilon}\dfrac{\overline{uw}}{r}\dfrac{\partial\overline{uv}}{\partial x}$ $-C_k\rho\dfrac{k}{\epsilon}\overline{w^2}\dfrac{\overline{uw}}{r^2}$

Wall-correction terms corresponding to the above two terms:

$$\Phi_{ij,1w} = C_1'\rho(\epsilon/k)\,[\overline{u_k u_m}\,n_k n_m\,\delta_{ij} - (3/2)\overline{u_k u_i}\,n_k n_j$$
$$- (3/2)\overline{u_k u_j}\,n_k n_i]f_\ell \qquad (6a)$$

$$\Phi_{ij,2w} = C_2'\rho\,[\Phi_{km,2}\,n_k n_m\,\delta_{ij} - (3/2)\Phi_{ik,2}\,n_k n_j$$
$$- (3/2)\Phi_{jk,2}\,n_k n_i]f_\ell \qquad (6b)$$

where $\ell = k$ with no summation implied, n_i is the i-directed unit vector normal to a wall (if present), and

$$f_\ell = \frac{C_\mu}{\kappa}\frac{k^{1.5}}{\epsilon}\frac{1}{x_\ell}$$

with x_1 and x_2 shown in Fig. 1.

The above wall corrections represent a "vectorial" generalization of forms suggested by Shir[15] and Gibson and Launder,[6] respectively.

The additive terms R_{ij} appearing in Eq. (3) arise from the transformation of the equations from plane to axially symmetric conditions and swirl, and are summarized in Table 2 in the form of contributions from convection, production, and diffusion.

Finally, the above stress model is closed by the equation governing the rate of turbulence-energy dissipation ϵ:

$$\frac{1}{r}\frac{\partial\rho r U_k\epsilon}{\partial x_k} = \frac{1}{r}\frac{\partial}{\partial x_k}\left(C_\epsilon r\rho\overline{u_k u_\ell}\frac{k}{\epsilon}\frac{\partial\epsilon}{\partial x_\ell}\right) + C_{D,1}\frac{\epsilon}{k}P_{kk} - C_{D,2}\rho\frac{\epsilon^2}{k}$$
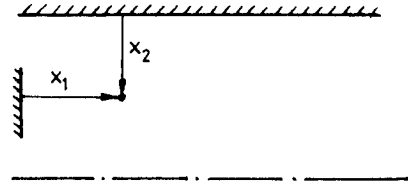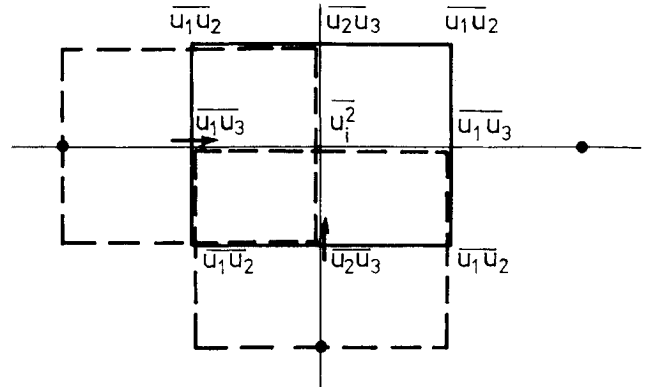
$$(7)$$

Fig. 1 Wall distances in function f_ℓ.

Fig. 2 Staggered stress arrangement.

Table 3 Turbulence-model constants

κ	C_μ	C_1	C_2	C_1'	C_2'	C_k	C_ϵ	$C_{D,1}$	$C_{D,2}$
0.42	0.09	1.8	0.6	0.5	0.3	0.22	0.18	1.44	1.92

The numerical values of the constants appearing in Eqs. (3-7) are given in Table 3.

Numerical Solution

Discretization of the transport equations governing mean and turbulence properties is based on the staggered finite-volume approach. The principles of this approach, as well as the underlying rationale for staggering the volumes pertaining to mass conservation and the momentum components U and V, are well known and will not be pursued here. A logical extension of the above rationale, previously used by Pope and Whitelaw[16] and adopted here, is to stagger the locations of the stresses and their associated volumes, as shown in Fig. 2. The main advantage of this practice is increased numerical stability—a result of the strong coupling established between the stresses and the associated "primary" strains. Focusing on the shear stress $\overline{u_1 u_2}$ as an example, it will be observed that this stress is located such that the discrete velocities used to approximate the strain $(\partial U/\partial r + \partial V/\partial x)$ straddle this stress centrally. A useful consequence of this practice is that the stresses are located such that no interpolation is involved in evaluating stress differences required for the finite-volume equations.

The convective fluxes appearing in the finite-volume equation are approximated by the power-law differencing scheme (PLDS) of Patankar[17] or, alternatively, by the quadratic upstream-weighted scheme (QUICK) of Leonard.[18] The latter has been used primarily in order to give added weight to the conclusion—based on computations with meshes having 24 × 24 and 48 × 48 nonuniformly distributed lines—that the coarser grid essentially supports a grid-independent solution, even with PLDS that is only first-order accurate and hence diffusive in the presence of flow-to-grid skewness. In the present application, however, skewness in the x-r plane is weak, and both schemes were found to return virtually indistinguishable solutions for both meshes. Grid independence will be demonstrated in the following section through a comparison of selected flow-property profiles.

The nondiffusive character of the quadratic scheme, combined with the absence of diffusive terms involving second-order derivatives, and the intense coupling between the swirl- and radial-momentum equations, necessitated a series of algorithmic measures to enhance numerical stability and hence convergence. One important measure, proposed by Huang and Leschziner,[19] involved the representation of a particular portion of each Reynolds stress by means of an associated apparent viscosity. As shown in Ref. 19, such a representation is offered by the discretized stress-transport equation that equates the stress to a group of additive contributions, one of which consists of a group of unconditionally positive quantities multiplying the primary strain associated with the stress in question.

A second measure that has been found to be helpful in a variety of recirculating flows entails a discrimination between positive and negative contributions to the source of any one discretized equation at all grid points and allocating the contributions according to

$$S_{ij} = S_{U,ij} + S_{P,ij}\,\overline{u_i u_j} \qquad \text{(no summation)} \qquad (8)$$

where S_U combines all the positive contributions and S_P all the negative ones.

Finally, a stabilizing relaxation of the coupling between the swirl- and radial-momentum equations during the iteration sequence has been introduced by adopting the representation of the centrifugal acceleration of Gosman et al.[20] in the V-momentum equation,

$$\left.\frac{\rho W^2}{r}\right|^{(m)} \rightarrow \left.\frac{\rho W^2}{r}\right|^{(m)} \left(1 + \frac{\alpha}{W^{(m-1)}}\,[V^{(m-1)} - V^{(m)}]\right) \qquad (9)$$

where (m) denotes the iteration level and α is an ad hoc numerical "relaxation parameter." The above is seen to become an identity when the iteration process has converged.
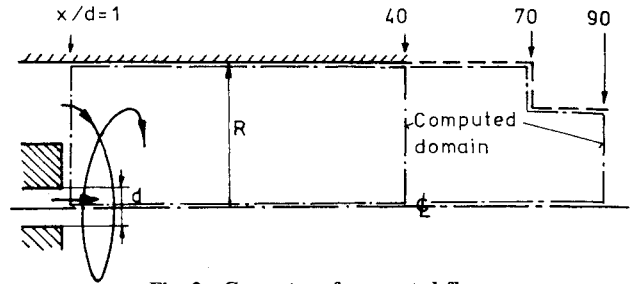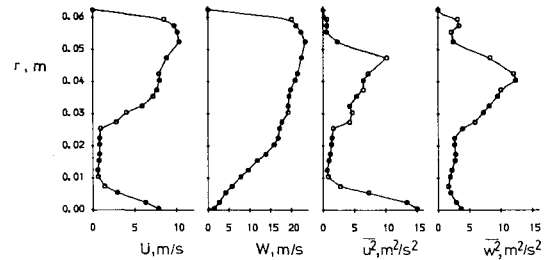

Fig. 3   Geometry of computed flow.

Fig. 4   Profiles of properties prescribed at the computational inlet plane $x/d = 1$.
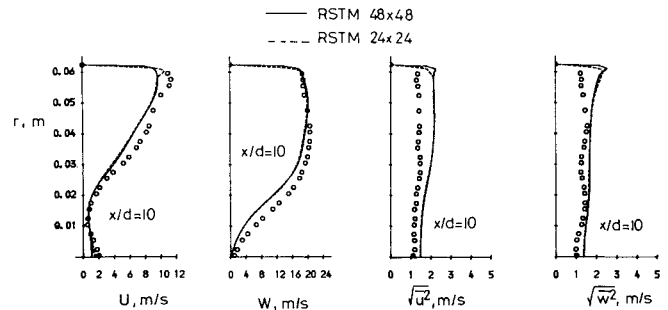

Fig. 5   Sensitivity of computed solution to grid-line density.

Application

The flow geometry for which calculations have been performed was examined experimentally by So et al.[5] and is shown in Fig. 3. A strongly swirling outer flow, characterized by the swirl parameter

$$S \equiv \frac{\int_0^R UWr^2\,dr}{R\int_0^R U^2 r\,dr} = 2.25 \qquad (10)$$

was directed into a uniform-diameter chamber of radius $R = 62.5$ mm together with a small central nonswirling jet of diameter $d = 8.7$ mm. The purpose of this jet was to delay the onset of reverse flow along the centerline beyond the measurement section that extends to $40d$. Without this jet, reverse flow, reflecting a "vortex breakdown," was found to occur at $12d$ from the inlet.

In all calculations presented here, the computational inlet plane was located at $x/d = 1$, which is the first downstream position at which measurements are available for U, W, $\overline{u^2}$, and $\overline{w^2}$; profiles of these quantities are given in Fig. 4. All remaining properties had to be estimated or assumed. Thus, the radial stress $\overline{v^2}$ was set equal to $\overline{w^2}$, whereas the three shear stresses were assumed to be zero. Coarse-grid tests in which the shear stresses were estimated by means of the Boussinesq stress-strain relationships resulted in insignificant changes to the solution. Finally, the inlet value for the dissipation rate ϵ was calculated from $\epsilon = k^{1.5}/(c_\mu^{-3/4}\ell_m)$—a relationship reflecting the assump-
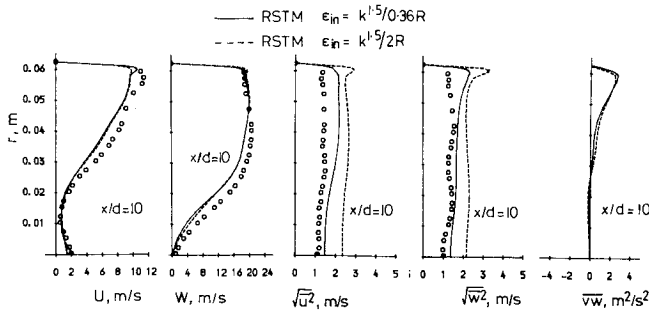
Fig. 6   Sensitivity of computed solution to the inlet level of ϵ (24 × 24 mesh).
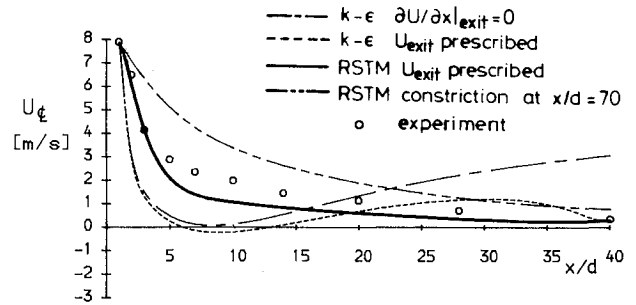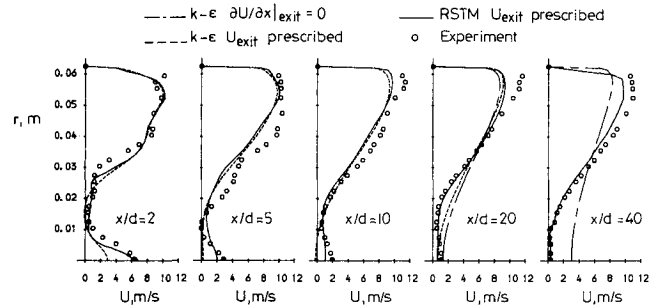

Fig. 7   Centerline velocity.

Fig. 8   Radial profiles of axial velocity.
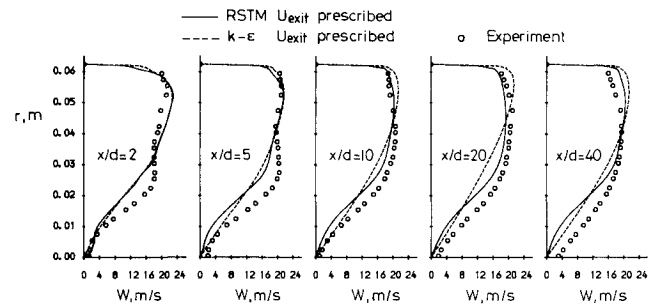

Fig. 9   Radial profiles of swirl velocity.

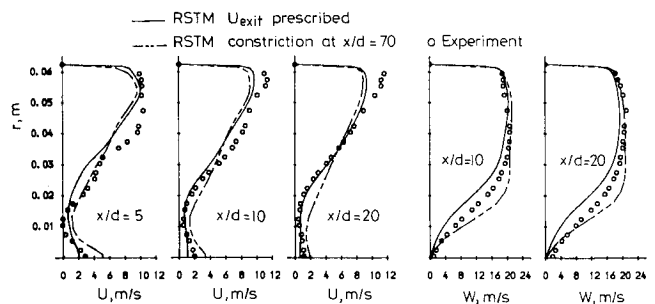Fig. 10   Radial profiles of axial and swirl velocity—effect of constriction at $x/d = 70$.

tion of turbulence-energy equilibrium, with ℓ_m being a mixing length whose value is considered below.

Computational results illustrating the sensitivity of the solution to mesh density and inlet level of ϵ are given in Figs. 5 and 6, respectively. Both figures compare corresponding profiles of U, W, $\overline{u^2}$, and $\overline{w^2}$ at a single location $x/d = 10$; the behavior observed at this location is wholly representative of that at others. Figure 5 demonstrates that increasing the mesh from 24 × 24 to 48 × 48 produced only marginal differences, except very close to the axis of symmetry and the wall. The most prominent feature is a peak in U velocity at the wall, returned by the coarse mesh due to a somewhat excessive distance between the near-wall mesh line and the wall—a region in which a log-law based treatment was adopted. The sensitivity to the inlet ϵ level was examined, using the 24 × 24 mesh, by varying ℓ_m between $0.06R$ and $0.34R$, and related results for the extreme ϵ levels are shown in Fig. 6. The influence of ϵ is seen to be largely confined to a modification of the normal-stress levels—a behavior expected from the explicit appearance of ϵ in the normal-stress Eq. (3). The lower level of ℓ_m is judged to be more realistic and is also observed to give good agreement with measured normal-stress data if used in conjunction with the stress closure. It is for these reasons that this lower level has been used in subsequent calculations discussed below.

Before attention is directed to a comparison between computations and experimental results, it is helpful, for the interpretation of the computed behavior, to dwell briefly on the implications of some of the experimentally observed flow features. It is thus noted from Fig. 7 that the marked tendency towards flow reversal, with the central jet present, strongly suggests that the flow is at least close to being "subcritical." Since the effect of the small jet is largely confined to a region close to the axis of symmetry, it may, in fact, be argued that the flow is likely to be subcritical in spite of the absence of reverse motion. Such a conclusion is certainly compatible with Squire's "rule-of-thumb"[21] according to which flows such as those considered here are likely to be subcritical if the ratio of maximum swirl velocity to mean axial velocity exceeds unity; in the present case, this ratio is approximately 2. A further indicator to the state of the flow may be extracted from the analysis presented by Benjamin for inviscid conditions. One outcome of this analysis is the relationship

$$\frac{J_0(2\omega_c r_a / U_o)}{J_1(2\omega_c r_a / U_o)} = -\frac{r_a U_o}{\omega_c (R^2 - r_a^2)} \quad (11)$$

which links, through the Bessel functions J_0 and J_1, the critical rotational speed ω_c of the inner vortex rotating in a solid-body-type manner to the average axial velocity in the outer region U_0, the duct radius R, and the radius r_a, at which the inner solid-body-rotational region merges with the outer one. Reference to the experimental velocity profiles shows that U_0, ω, and r_a can be estimated with fair accuracy, and when the first two values are inserted into Benjamin's relationship, one solution for the critical rotational speed ω_c is found to be very close to the experimental value ω.

Computational results are presented, mostly in comparison with experimental data, in Figs. 7-15. Unless otherwise stated, the solutions have been obtained with the 48 × 48 mesh. First, Fig. 7 shows the variation of the centerline velocity resulting from four of a total of five computations made—two with the k-ϵ model and three with the stress closure. For each model, one computation was performed with the exit condition $\partial U/\partial x = 0$, whereas in the second the exit U profile was prescribed explicitly. In the fifth computation, made with the stress model, the solution domain was extended to $x/d = 90$, and a flow-

accelerating sudden constriction was placed at $x/d = 70$, for reasons discussed later.

The first exit condition is the one usually used in calculations of confined recirculating flows on the assumption that the flow tends towards a fully established state at the exit plane that is arranged to be remote from the separation zone. With this condition imposed, Fig. 7 shows that the $k-\epsilon$ model predicts a rapid decay of centerline velocity due to a diffusive erosion of the central jet, followed by a re-establishment zone in which the centerline velocity rises towards the level prevailing in an ordinary pipe flow. This is clearly contrary to the measured behavior that shows no recovery and an indefinite tendency towards flow reversal. It is interesting to mention here that Wilhelmi,[22] who has computed a flow displaying subcritical features with the $k-\epsilon$ model, also observed the model to predict, contrary to his own experimental measurements, flow re-establishment towards the exit. By considering profiles of velocity and stresses, it will be shown shortly that the misrepresentation returned by the $k-\epsilon$ model is a direct consequence of its failure to account for swirl-induced turbulence damping. The center-line velocity emerging from the stress-model calculation with the same exit condition has not been included in Fig. 7, for in this case the solution did not fully converge and contained a large reverse-flow region across a significant portion of the radius, extending from $x/d = 15$ right up to the exit plane. This
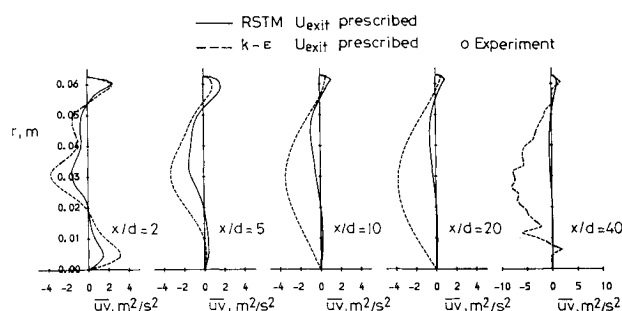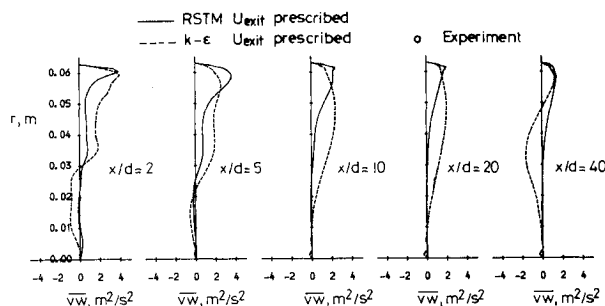

Fig. 11   Radial profiles of shear stress $\overline{uv}$.

Fig. 12   Radial profiles of shear stress $\overline{vw}$.

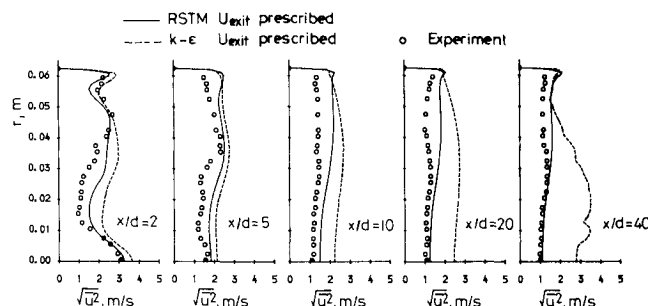Fig. 13   Radial profiles of axial turbulence intensity.

behavior may arguably suggest an overestimation of swirl-induced turbulence attenuation, but no definite statement can be made since the boundary condition $\partial U/\partial x = 0$ at the exit plane is clearly inappropriate if fluid re-enters the flow domain through this plane.

It is precisely for this reason that the above computations were repeated with the exit velocity prescribed. Although this must be viewed as an unsatisfactory measure from a practical point of view, it is useful for the present purpose of assessing turbulence-model performance. As shown in Fig. 7, the $k-\epsilon$ model persists in predicting a recovery after an initial fast decay but is, of course, ultimately forced to return a reduction in the centerline velocity so as to satisfy the prescribed exit condition. The stress model, in contrast, yields a continuous decay and predicts that a change in the exit condition affects the centerline velocity throughout the flow domain. An important implication of this comparison is, therefore, that the $k-\epsilon$ model fails to capture the subcritical nature of the flow, whereas the stress closure appears to represent the primary flow features correctly.

Additional support for the latter conclusion is provided by the fifth calculation (made with a 24×50 grid) involving a flow constriction of area ratio 0.75 extending from $x/d = 70$ to 90. This was motivated by the desire to relax the previous exit treatment and by Escudier's observation that the structure of subcritical flows is highly sensitive to "downstream control" effected by downstream constrictions. In the knowledge that the stress closure appeared to capture the subcritical nature of the flow, the objective was, therefore, to examine whether the disturbance created by the constriction would propagate upstream and possibly "simulate" the conditions achieved by prescribing the U profile at $x/d = 40$. As seen from Fig. 7, introduction of the constriction results in the high level of sensitivity expected from a subcritical flow, and although not reproducing correctly the experimental rate of decay of the centerline velocity, it prevents reverse flow at $x/d = 40$.

A more detailed view of the relative performance of the turbulence models can be gained from Figs. 8 and 9 showing, respectively, comparisons of axial- and swirl-velocity profiles returned by computations in which the axial exit velocity was prescribed. In the last two plots of Fig. 8, the U-velocity profiles computed with the $k-\epsilon$ model and the condition $\partial U/\partial x = 0$ have been included in order to highlight the previously mentioned flow recovery predicted by this model. All other U profiles for the above condition—as well as those for W—closely resemble corresponding ones shown in Figs. 8 and 9 for the prescribed exit profile. Moreover, as shown in Fig. 10, use of the constriction at $x/d = 70$ yields similar profiles to those obtained with the prescribed exit velocity, and attention is, therefore, focused on results obtained with the latter condition. Figures 8 and 9 both imply that the $k-\epsilon$ model seriously overestimates the diffusive transport of momentum in the radial direction, a defect that appears to be the cause for the failure of the model to capture the subcritical nature of the flow. This is clearly reflected by a flattening of U profiles and an excessive tendency of the swirl velocity to assume a solid-body profile. In contrast, the stress model maintains the correct shape of both U and W profiles and clearly mimics the existence of two rotational regimes—the inner close to a forced vortex and the outer combining forced- and free-vortex motion.

Although there are no experimental data available for the shear stresses, the comparison shown in Figs. 11 and 12 between computed $k-\epsilon$ and Reynolds-stress-transport model (RSTM) profiles brings out well the fact that the differences observed in Figs. 7–9 must be rooted in the drastic reduction of the shear-stress level produced by the RSTM in response to swirl-induced strains. That such a reduction is unlikely to be grossly excessive is implied by Figs. 13 and 14 that show that the predicted levels of the turbulence intensities $\sqrt{\overline{u^2}}$ and $\sqrt{\overline{w^2}}$ are in fair agreement with those measured. It is interesting to note that, although the RSTM, expectedly, returns depressed levels of the above intensities, as well as for the radial intensity $\sqrt{\overline{v^2}}$
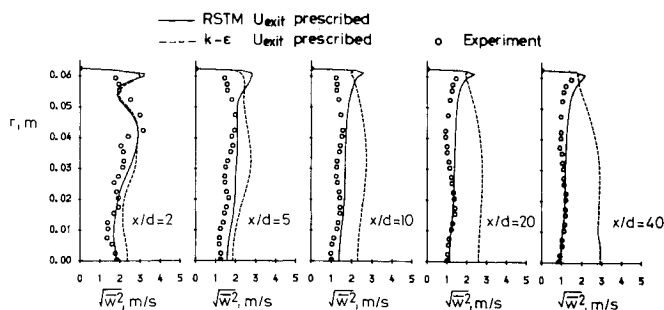
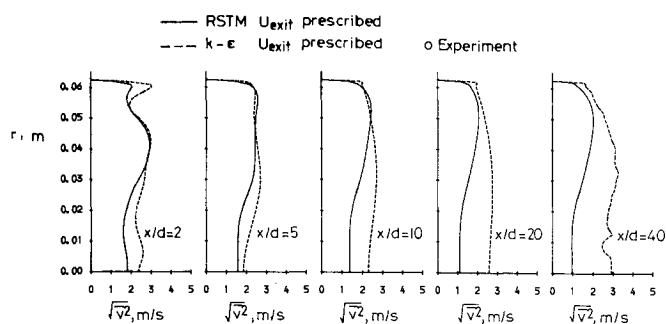Fig. 14 Radial profiles of circumferential turbulence intensity.

Fig. 15 Radial profiles of radial turbulence intensity.

shown in Fig. 15, the levels are similar so that, somewhat unexpectedly, anisotropy is not marked. This suggests that the primary process responsible for the strong shear-stress reduction shown in Figs. 11 and 12 is not the low level of production—which would occur if v^2 were low—but pressure-strain redistribution that is represented by "sinks" in the shear-stress equations. This is a somewhat disconcerting conclusion, for the primary strength of stress closures is generally seen to lie in the exact representation of stress production that is held to largely control the stress levels. In this case, the pressure-strain model —a rather weak element in the closure as a whole—appears to be in control. On the other hand, it may be argued, optimistically, that the observed performance of the stress model encourages a degree of confidence in the validity of the pressure-strain representation.

Conclusions

A finite-volume procedure has been used in conjunction with a Reynolds-stress transport model to compute a strongly swirling confined flow. As a result of a severe swirl-induced reduction of turbulent mixing, the flow displays unusual features akin to those observed in subcritical free-surface flow.

The computations presented show that the Reynolds-stress model captures these features, whereas the isotropic-viscosity $k-\epsilon$ model does not. Specifically, the former correctly represents the physically realistic sensitivity of the flow to disturbances introduced far downstream. However, this very quality makes the computational treatment of the flow-exit plane problematic and necessitated the explicit prescription of the experimental axial velocity across this plane.

The calculations show that the drastic differences in performance between the $k-\epsilon$ model and the stress closure are rooted in the much lower levels of shear stresses returned by the latter in response to swirl-related streamline curvature. Somewhat surprisingly, this reduction is not found to be related to a significant anisotropy involving a low level of the radial turbulence intensity $\sqrt{v^2}$ relative to the other two normal intensities, but appears to be due to the influence of the pressure-strain model on the shear stresses.

References

[1]Benjamin, T. B., "Theory of the Vortex Breakdown Phenomenon," *Journal of Fluid Mechanics,* Vol. 14, Pt. 4, Dec. 1962, pp. 593-629.

[2]Benjamin, T. B., "Significance of the Vortex Breakdown Phenomenon," *ASME Journal of Basic Engineering,* Vol. 87, Pt. 2, June 1965, pp. 518-524.

[3]Escudier, M. P. and Keller, J. J., "Recirculation in Swirling Flow: A Manifestation of Vortex Breakdown," *AIAA Journal,* Vol. 23, Jan. 1985, pp. 111-116.

[4]Jones, W. P. and Wilhelmi, J., "Isothermal Measurements in a Confined Swirl-Driven Recirculating Flow," *Proceedings of the International Symposium on Applications of Laser-Doppler Anemometry to Fluid Mechanics,* Lisbon, Portugal, Paper 10.4, 1982.

[5]So, R. M., Ahmed, S. A., and Mongia, H. C., "An Experimental Investigation of Gas Jets in Confined Swirling Air Flow," NASA CR-3832, 1984.

[6]Gibson, M. M. and Launder, B. E., "Ground Effects on Pressure Fluctuations in the Atmospheric Boundary Layer," *Journal of Fluid Mechanics,* Vol. 86, Pt. 3, April 1978, pp. 491-511.

[7]Launder, B. E., Reece, G. J., and Rodi, W., "Progress in the Development of a Reynolds Stress Turbulence Closure," *Journal of Fluid Mechanics,* Vol. 68, Pt. 3, April 1975, pp. 537-566.

[8]Launder, B. E., "An Improved Algebraic Stress Model of Turbulence," Imperial College, London, Mechanical Engineering Dept., Rept. TM/TN/A/9, 1971.

[9]Rodi, W., "The Prediction of Free Turbulent Boundary Layers by Use of a Two-Equation Turbulence Model," Ph.D. Thesis, Univ. of London, 1972.

[10]Boysan, F., Weber, R., and Swithenbank, J., "Modeling Coal-Fired Cyclone Combustors," *Combustion and Flame,* Vol. 63, Pt. 1 & 2, Jan.-Feb. 1986, pp. 73-86.

[11]Truelove, J. S. and Mahmud, T., "Calculation of Strongly Swirling Jet Flow," *Proceedings of the 9th Australasian Fluid Mechanics Conference,* Univ. of Auckland, Auckland, New Zealand, 1986, pp. 462-469.

[12]Boysan, F., Zhou, T., Vasquz-Malebran, S., and Swithenbank, J., "Calculation of Turbulent Swirling Flows with a Second-Order Reynolds Stress Closure," Univ. of Sheffield, Sheffield, England, Rept. HIJ450, 1985.

[13]Fu, S., Huang, P. G., Launder, B. E., and Leschziner, M. A., "A Comparison of Algebraic and Differential Second-Moment Closures for Axisymmetric Turbulent Shear Flows With and Without Swirl," *Journal of Fluid Engineering,* Vol. 110, 1988, pp. 216-221.

[14]Launder, B. E. and Spalding, D. B., "The Numerical Computation of Turbulent Flows," *Computer Methods in Applied Mechanics and Engineering,* Vol. 3, Pt. 3, May 1974, pp. 269-289.

[15]Shir, C. C., "A Preliminary Numerical Study of Atmospheric Turbulent Flows in the Idealized Planetary Boundary Layer," *Journal of Atmospheric Sciences,* Vol. 30, Pt. 7, Oct. 1973, pp. 1327-1339.

[16]Pope, S. B. and Whitelaw, J. H., "The Calculation of Near Wake Flows," *Journal of Fluid Mechanics,* Vol. 73, Pt. 1, Jan. 1976, pp. 9-32.

[17]Patankar, S. V., *Numerical Heat Transfer and Fluid Flow,* McGraw-Hill, New York, 1980.

[18]Leonard, B. P., "A Stable and Accurate Convective Modeling Procedure Based on Quadratic Upstream Interpolation," *Computer Methods in Applied Mechanics and Engineering,* Vol. 19, Pt. 1, June 1979, pp. 59-98.

[19]Huang, P. G. and Leschziner, M. A., "Stabilization of Recirculating-Flow Computations Performed with Second-Moment Closures and Third-Order Discretization," *Proceedings of the 5th International Symposium on Turbulent Shear Flows,* Cornell, 1985, pp. 20.7-20.12.

[20]Gosman, A. D., Koosinlin, M. L., Lockwood, F. C., and Spalding, D. B., "Transfer of Heat in Rotating Systems," American Society of Mechanical Engineering, New York, Paper 76-GT-25, 1976.

[21]Squire, H. B., "Analysis of the 'Vortex Breakdown' Phenomenon," *Miszellanen der Angewandten Mechanik,* Akademie, Berlin, 1962, pp. 306-312.

[22]Wilhelmi, J., "Axisymmetric Swirl Stabilized Combustion," Ph.D. Thesis, Univ. of London, London, 1984.